

Periapsis shifts in dark matter distribution around a black hole

Takahisa Igata,^{1,2,*} Tomohiro Harada,^{3,†} Hiromi Saida,^{4,‡} and Yohsuke Takamori^{5,§}

¹*Department of Physics, Gakushuin University,*

Mejiro, Toshima, Tokyo 171-8588, Japan

²*KEK Theory Center, Institute of Particle and Nuclear Studies,*

High Energy Accelerator Research Organization, Tsukuba 305-0801, Japan

³*Department of Physics, Rikkyo University, Toshima, Tokyo 171-8501, Japan*

⁴*Daido University, Nagoya, Aichi 457-8530, Japan*

⁵*National Institute of Technology (KOSEN),*

Wakayama College, Gobo, Wakayama 644-0023, Japan

(Dated: December 8, 2023)

We consider the periapsis shifts of bound orbits of stars on static clouds around a black hole. The background spacetime is constructed from a Schwarzschild black hole surrounded by a static and spherically symmetric self-gravitating system of massive particles, which satisfies all the standard energy conditions and physically models the gravitational effect of dark matter distribution around a nonrotating black hole. Using nearly circular bound orbits of stars, we obtain a simple formula for the precession rate. This formula explicitly shows that the precession rate is determined by a positive contribution (i.e., a prograde shift) from the conventional general-relativistic effect and a negative contribution (i.e., a retrograde shift) from the local matter density. The four quantities for such an orbit (i.e., the orbital shift angle, the radial oscillation period, the redshift, and the star position mapped onto the celestial sphere) determine the local values of the background model functions. Furthermore, we not only evaluate the precession rate of nearly circular bound orbits in several specific models but also simulate several bound orbits with large eccentricity and their periapsis shifts. The present exact model demonstrates that the retrograde precession does not mean any exotic central objects such as naked singularities or wormholes but simply the existence of significant energy density of matters on the star orbit around the black hole.

I. INTRODUCTION

We are currently in the midst of rapid progress in observing the vicinity of black holes. In particular, in the observation of the center of our galaxy, the orbital evolution of the so-called

* takahisa.igata@gakushuin.ac.jp

† harada@rikkyo.ac.jp

‡ saida@daido-it.ac.jp

§ takamori@wakayama-nct.ac.jp

S-stars orbiting a supermassive black hole candidate, Sagittarius A* (Sgr A*), has been actively investigated [1, 2]. Because S-stars can be regarded as test particles on the gravitational field of Sgr A*, precise measurements of their orbital evolution provide information on the central object and its surrounding matters, as well as on the spacetime geometry [3–5].

A theoretical understanding of such orbital evolution is essential for identifying observables and interpreting observational results. One of the typical examples is that the elliptic orbit, well-known in Newtonian gravity, rotates in the same direction as the orbital evolution because of the general-relativistic effect (see, e.g., Ref. [6]). This is the so-called periapsis shift phenomenon of the bound orbits. Thus, by observing the displacement of the orbit due to this precessional motion, we can estimate the general-relativistic correction to the gravitational field. Furthermore, it has been discussed that supermassive and intermediate-mass black holes may be associated with large dark matter overdensities, called density spikes of dark matter [7–10] and an ultralight dark matter solitons [11]. Obviously, the contribution from extended mass distribution must also be considered as a correction to the black hole gravitational field. However, although it has been discussed in post-Newtonian gravity [12] and by the general-relativistic Plummer model [13], the effect of matter distribution on the periapsis shift phenomena is still controversial in the framework including a general-relativistic black hole. Therefore, the most important next issue is to clarify the competition between the general-relativistic and local-density effects on the periapsis shift in a spacetime where a black hole and matter distribution are coexistent. Such knowledge will broaden our understanding of the effects of matter fields on particle dynamics in the strong gravity regime. Besides, it will be useful for comparison with the case where the center is not a black hole but an exotic object [14–16].

To clarify the above issues, we construct a background spacetime with a static and spherically symmetric distribution of massive particles around the Schwarzschild black hole by exactly solving the Einstein equations. Applying a method developed by Einstein [17, 18], we obtain a black hole spacetime surrounded by matter distribution known as an Einstein cluster, which consists of an averaged distribution of collisionless particles. Then, utilizing this black hole spacetime, we aim to formulate the competition between the general-relativistic and local-density effects that determine the direction of the periapsis shift of the bound geodesic orbits of stars on the matter distribution. Using this formulation, we consider the case in general relativity where the retrograde shift due to extended matter distribution can compensate for the prograde shift due to the general-relativistic effect (see Refs. [12, 19–21] for the post-Newtonian regime). However, it is not obvious whether extended matter distribution contributes to the retrograde shift in any case. Therefore, it is quite

important to discuss the periapsis shift by considering the standard energy conditions and other physically reasonable conditions for the matter field.

Here, we review recent progress in black hole spacetimes involving matter distribution constructed by what we call the Einstein cluster approach, a method for obtaining solutions to the Einstein equations in which the matter distribution has a stress-energy tensor of the same type as the Einstein clusters. As Boehmer and Harko [22] and Lake [23] showed, an Einstein cluster was a possible galactic dark matter halo model. Using the Einstein cluster approach, Cardoso *et al.* recently proposed a self-consistent black hole model immersed in a whole galactic halo with a Hernquist-type profile [24]. The effects of the halo on the innermost stable circular orbit, black hole shadow, and gravitational quasi-normal modes [24]; electromagnetic quasi-normal modes [25]; and the epicyclic resonance of quasi-periodic oscillations in active galactic nuclei [26] were discussed. Later, using a matter field subjected to a different equation of states, Jusufi proposed other exact solutions and considered the effect of black hole shadows and the stability of particle orbits [27]. More recently, Figueiredo *et al.* developed a geometry with two density profiles to compare with the Hernquist-type profile, revealing variations of geodesic motion and gravitational wave fluxes and these model-independent nature [28].

We should clarify the characteristics of our model compared to the previous models. The idea of using the Einstein cluster approach to surround a black hole with a matter field is common to these previous studies. Note, however, that the model in Ref. [24] has a serious problem in its physical interpretation because it violates the dominant energy condition near the black hole, whereas, in the current paper, we improve the model so that it can satisfy all of the dominant, weak, null, and strong energy conditions over the entire region.

This paper is organized as follows. In Sec. II, we review a static and spherically symmetric cloud solution to the Einstein equations. In particular, we construct a black hole surrounded by a static Einstein cluster and clarify physically reasonable constraints based on the standard energy conditions. In Sec. III, we formulate the dynamics of a freely falling particle in the Einstein cluster around a black hole and show the conditions for the existence of nearly circular bound orbits. Then, we derive a formula that shows how the conflicting general-relativistic and local-density effects determine the precession rate that characterizes the periapsis shift. In Sec. IV, we evaluate the precession rate for nearly circular orbits in several spacetime models obtained by giving concrete forms to the metric functions. Furthermore, we demonstrate periapsis shifts of bound orbits with large eccentricity. In Sec. V, we discuss how to determine the matter distribution around a black hole using the formula, given observational data on the orbiting stars. Section VI is devoted to a

summary and discussion. We use units in which $G = 1$ and $c = 1$.

II. STATIC CLOUDS AROUND THE SCHWARZSCHILD BLACK HOLE

We review a static and spherically symmetric cloud solution to the Einstein equations. Let t be a static time, and r be the areal radius. The labels (θ, φ) are the standard spherical coordinates. Using these coordinates $x^\mu = (t, r, \theta, \varphi)$, we consider the general metric ansatz of static and spherically symmetric spacetimes,

$$g_{\mu\nu} dx^\mu dx^\nu = - \left(1 - \frac{2\alpha(r)}{r}\right) dt^2 + \left(1 - \frac{2m(r)}{r}\right)^{-1} dr^2 + r^2(d\theta^2 + \sin^2\theta d\varphi^2), \quad (1)$$

where $\alpha(r)$ and $m(r)$ are continuous functions of r , and in particular $m(r)$ is the Misner-Sharp mass [29, 30]. Now we assume that

$$0 \leq m < \frac{r}{2}, \quad (2)$$

$$\alpha < \frac{r}{2}. \quad (3)$$

Before assuming the Einstein cluster of collisionless particles, we review the Einstein cluster approach, a method for obtaining solutions to the Einstein equations in which the matter distribution has a stress-energy tensor of the same type as the Einstein clusters. We consider the following form of the stress-energy tensor:

$$T^\mu{}_\nu = \text{diag}(-\epsilon, 0, \Pi, \Pi), \quad (4)$$

where ϵ and Π denote energy density and tangential pressure, respectively, and we assume that the radial pressure vanishes. Through the Einstein equations, ϵ and Π are related to m as

$$\epsilon(r) = \frac{m'}{4\pi r^2}, \quad (5)$$

$$\Pi(r) = \frac{m}{2(r-2m)}\epsilon(r), \quad (6)$$

and the vanishing radial pressure leads to the remaining nontrivial equation

$$\alpha' = \frac{1}{2} \left(1 - \frac{r-2\alpha}{r-2m}\right) = \frac{\alpha-m}{r-2m}, \quad (7)$$

or equivalently,

$$m = \frac{\alpha - \alpha' r}{1 - 2\alpha'}, \quad (8)$$

where the prime denotes differentiation with respect to r . As m and α are continuous, the function α' is also continuous. Note that Eq. (7) together with the inequalities (2) and (3) implies that

$$\alpha' < \frac{1}{2}. \quad (9)$$

Consequently, for given $m(r)$ and $\alpha(r)$ under the constraints (2) and (3), we can specify the matter distribution $\epsilon(r)$ and $\Pi(r)$ through Eqs. (5) and (6), respectively. This static configuration is possible by a balance between the gravitational force and the tangential pressure.

For a matter field to be physically reasonable, the stress-energy tensor must satisfy several energy conditions (see, e.g., Ref. [31]). Imposing the energy conditions further restricts m and α than Eqs. (2) and (3). Some of the energy conditions for $T^\mu{}_\nu$ are written as follows: (i) weak energy condition, $\epsilon \geq 0$ and $\epsilon + \Pi \geq 0$; (ii) strong energy condition, $\epsilon + 2\Pi \geq 0$ and $\epsilon + \Pi \geq 0$; (iii) null energy condition, $\epsilon \geq 0$ and $\epsilon + \Pi \geq 0$; and (iv) dominant energy condition, $\epsilon \geq |\Pi|$. For the vacuum region (i.e., $\epsilon = 0$ and $\Pi = 0$), all these energy conditions are trivially satisfied, and thus, $m' = 0$ holds. For the nonvacuum region, Conditions (i)–(iii) under the inequality (2) provide a common inequality, $m' > 0$. On the other hand, Condition (iv) can be reduced to $m' > 0$ and $0 < m \leq 2r/5$. This means that if a black hole with mass M_0 is centered and a matter exists in the region $r < 2.5M_0$, then the violation of the dominant energy condition necessarily occurs there. Therefore, if a matter distribution surrounding the black hole satisfies all the standard energy conditions, a vacuum region must exist between the horizon and the inner boundary of the distribution. Note that if any one of the energy conditions is imposed together with the assumption (2), the quantities ϵ and Π will be positive.

The Einstein cluster [17, 18] is a physical model compatible with the above $T^\mu{}_\nu$. This cluster is static and spherically symmetric and consists of an averaged distribution of collisionless particles. The motion of each particle in the cluster is circular geodesic motion. The counterrotating particles cancel out their angular momenta, so that the spherical symmetry is recovered. Let $n(r)$ and $L_p(r)$ be the proper number density of counterrotating particles with rest mass m_p and the total angular momentum of each of the particles moving on a circular geodesic with radius r , respectively. Then, as summarized in Appendix A, the stress-energy tensor $T^\mu{}_\nu$ is free from radial pressure and coincides with Eq. (4), where

$$\epsilon = m_p n(r) \left(1 + \frac{l_p^2}{r^2} \right) = m_p n(r) \frac{r - 2m}{r - 3m}, \quad (10)$$

$$\Pi = m_p n(r) \frac{l_p^2}{2r^2} = \frac{1}{2} \frac{l_p^2}{r^2 + l_p^2} \epsilon(r) = m_p n(r) \frac{m}{2(r - 3m)}, \quad (11)$$

where $l_p = L_p/m_p$. These expressions imply that $\epsilon \geq 0$ and $\Pi \geq 0$, and therefore, m is further restricted as

$$0 \leq m < \frac{r}{3} \quad \text{and} \quad m' \geq 0. \quad (12)$$

Furthermore, these restrictions with Eq. (8) lead to

$$\alpha' r \leq \alpha < (1 + \alpha') \frac{r}{3} \quad \text{and} \quad \alpha'' \leq 0, \quad (13)$$

where we have used the relation

$$m' = -\frac{(r - 2\alpha)\alpha''}{(1 - 2\alpha')^2}. \quad (14)$$

Therefore, we see that the Einstein cluster automatically satisfies all of the above energy conditions. To obtain an Einstein cluster, we need to give either m and α so that the inequalities (12) and (13) hold.

Hereafter, we particularly focus on a black hole surrounded by the Einstein cluster of collisionless particles. We assume that the mass function m is of the form

$$m = \begin{cases} M_0 & \text{for } 2M_0 < r \leq r_{\min}, \\ m_*(r) & \text{for } r_{\min} \leq r \leq r_{\max}, \\ M & \text{for } r \geq r_{\max}, \end{cases} \quad (15)$$

$$m = \begin{cases} m_*(r) & \text{for } r_{\min} \leq r \leq r_{\max}, \end{cases} \quad (16)$$

$$m = \begin{cases} M & \text{for } r \geq r_{\max}, \end{cases} \quad (17)$$

where M_0 , M , r_{\min} , and r_{\max} are positive constants, and $m_*(r)$ is a continuous mass function of r and must satisfy

$$m_*(r_{\min}) = M_0, \quad (18)$$

$$m_*(r_{\max}) = M. \quad (19)$$

This model is known as the thick Einstein shell [32]. Figure 1 shows a schematic picture of a black hole with mass M_0 surrounded by an Einstein cluster distributed in the region $r_{\min} \leq r \leq r_{\max}$. Then the corresponding α can be obtained by solving Eq. (7) as¹

$$\alpha(r) = \begin{cases} \frac{r}{2} - \frac{C_0^2}{2}(r - 2M_0) & \text{for } 2M_0 < r \leq r_{\min}, \\ \alpha_*(r) & \text{for } r_{\min} \leq r \leq r_{\max}, \\ \frac{r}{2} - \frac{C^2}{2}(r - 2M) & \text{for } r \geq r_{\max}, \end{cases} \quad (21)$$

$$\alpha(r) = \begin{cases} \alpha_*(r) & \text{for } r_{\min} \leq r \leq r_{\max}, \end{cases} \quad (22)$$

$$\alpha(r) = \begin{cases} \frac{r}{2} - \frac{C^2}{2}(r - 2M) & \text{for } r \geq r_{\max}, \end{cases} \quad (23)$$

¹ If we first assume the form of m , then g_{tt} is restricted by the continuity of the metric at $r = r_{\min}$ to the following form:

$$g_{tt} = -\frac{r_{\min} - 2M_0}{r} \exp \left[\int_{r_{\min}}^r \frac{d\tilde{r}}{\tilde{r} - 2m(\tilde{r})} \right]. \quad (20)$$

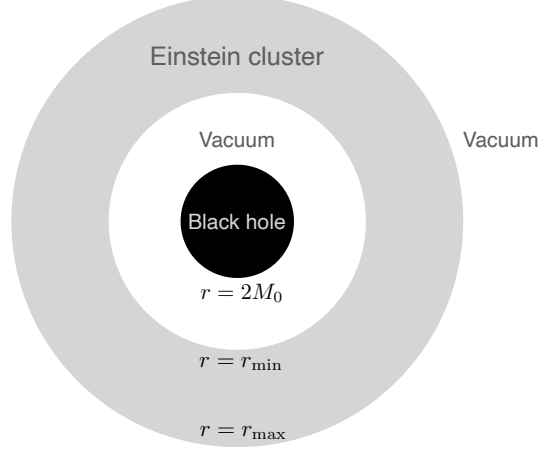


FIG. 1. Schematic picture of a black hole with mass M_0 surrounded by an Einstein cluster distributed in the region $r_{\min} \leq r \leq r_{\max}$.

where C_0 and C are integral constants, and $\alpha_*(r)$ is a continuous function of r and must satisfy

$$\alpha_*(r_{\min}) = \frac{r_{\min}}{2} - \frac{C_0^2}{2}(r_{\min} - 2M_0), \quad (24)$$

$$\alpha_*(r_{\max}) = \frac{r_{\max}}{2} - \frac{C^2}{2}(r_{\max} - 2M). \quad (25)$$

In the region $2M_0 < r \leq r_{\min}$, the metric (1) is reduced to the Schwarzschild spacetime with mass M_0 ,

$$ds^2 = -(1 - 2M_0/r) d\tilde{t}^2 + (1 - 2M_0/r)^{-1} dr^2 + r^2(d\theta^2 + \sin^2\theta d\varphi^2), \quad (26)$$

where $\tilde{t} = C_0 t$ is the Schwarzschild time. Thus, M_0 is the mass of the central black hole. In the region $r \geq r_{\max}$, the metric (1) is reduced to the Schwarzschild spacetime with mass M ,

$$ds^2 = -(1 - 2M/r) dT^2 + (1 - 2M/r)^{-1} dr^2 + r^2(d\theta^2 + \sin^2\theta d\varphi^2), \quad (27)$$

where $T = Ct$ is the Schwarzschild time. If we set $C = 1$, the time t is the proper time for asymptotic static observers. Thus, M is the sum of the masses of the black hole and the matter (i.e., the Arnowitt-Deser-Misner mass).

To obtain the distribution of an Einstein cluster, we must impose the inequalities (12), or equivalently,

$$0 < m_* < \frac{r}{3}, \quad m'_* > 0. \quad (28)$$

The second inequality $m_* < r/3$ evaluated at $r = r_{\min}$ and $r = r_{\max}$ provides lower bounds of r_{\min}

and r_{\max} , respectively,

$$r_{\min} > 3M_0, \quad (29)$$

$$r_{\max} > 3M. \quad (30)$$

Therefore, our Einstein cluster satisfying all the standard energy conditions inevitably shows a vacuum region at least in $r < 3M_0$. Considering the stability of the Einstein clusters, we hereafter assume $r_{\min} > 6M_0$ in almost all setups. We also obtain $M > M_0$ because of the third inequality $m'_* > 0$.

III. STELLAR DYNAMICS IN AN EINSTEIN CLUSTER AROUND A BLACK HOLE

We consider stellar dynamics in an Einstein cluster around a black hole. We assume that the matter field contributes to the particle motion only through the gravitational field and that local interactions between the star and the density distribution (e.g., pressure, friction, etc.) are negligible. The Lagrangian of a massive particle with unit mass is given by

$$\mathcal{L} = \frac{1}{2} \left[- \left(1 - \frac{2\alpha}{r} \right) \dot{t}^2 + \left(1 - \frac{2m}{r} \right)^{-1} \dot{r}^2 + r^2 \dot{\theta}^2 + r^2 \sin^2 \theta \dot{\varphi}^2 \right], \quad (31)$$

where the dot denotes differentiation with respect to proper time. Without loss of generality, we assume from spherical symmetry that a freely falling particle moves on the equatorial plane $\theta = \pi/2$. Since t and φ are cyclic variables in this mechanical system, the conjugate momenta are conserved,

$$\frac{\partial \mathcal{L}}{\partial \dot{t}} = - \left(1 - \frac{2\alpha}{r} \right) \dot{t} = -E, \quad (32)$$

$$\frac{\partial \mathcal{L}}{\partial \dot{\varphi}} = r^2 \dot{\varphi} = L, \quad (33)$$

where E and L are constant energy and angular momentum per unit mass of a particle, respectively.

The remaining Euler-Lagrange equation for r is written as

$$\ddot{r} + V' = 0, \quad (34)$$

$$V(r) = \frac{1}{2} \left(1 - \frac{2m}{r} \right) \left(\frac{L^2}{r^2} + 1 \right) - \frac{r - 2m}{r - 2\alpha} \frac{E^2}{2}, \quad (35)$$

where the prime denotes differentiation with respect to r , and we have used Eqs. (32), (33), and the normalization for the four-velocity, $\mathcal{L} = -1/2$. Integrating Eq. (34), we obtain

$$\frac{1}{2} \dot{r}^2 + V = 0, \quad (36)$$

which corresponds to the normalization condition in terms of E and L .

We focus on circular orbits, where particles must satisfy the stationary conditions

$$\dot{r} = 0 \quad \text{and} \quad \ddot{r} = 0. \quad (37)$$

Through Eqs. (34) and (36), these conditions are rewritten as

$$V = 0 \quad \text{and} \quad V' = 0. \quad (38)$$

Solving these algebraic equations for L and E , we obtain angular momentum and energy for circular orbits as functions of the orbital radius,

$$L^2(r) = \frac{mr^2}{r - 3m}, \quad (39)$$

$$E^2(r) = \left(1 - \frac{2\alpha}{r}\right) \frac{r - 2m}{r - 3m}, \quad (40)$$

respectively. These expressions imply that the circular orbits only exist in the range

$$r - 3m > 0. \quad (41)$$

The circular orbits are stable if $V'' > 0$, marginally (un)stable if $V'' = 0$, and unstable if $V'' < 0$, where V'' is the second derivative of V on circular orbits given by

$$V'' = \frac{(r - 6m)m + m'r^2}{r^3(r - 3m)}, \quad (42)$$

where Eqs. (39) and (40) were used to eliminate L^2 and E^2 , respectively.

We consider bound orbits that are nearly circular orbits, i.e., motion of a particle which is displaced slightly from the equilibrium radius of a stable circular orbit. For sufficiently small displacement, we can introduce two frequencies

$$\omega_\varphi = \dot{\varphi} = \sqrt{\frac{m}{r^2(r - 3m)}}, \quad (43)$$

$$\omega_r = \sqrt{V''}, \quad (44)$$

where ω_φ is the angular frequency, and ω_r is the frequency of radial harmonic oscillation. The periapsis shift of the nearly circular orbits is measured by the precession rate

$$\nu = \frac{\omega_\varphi - \omega_r}{\omega_\varphi} \quad (45)$$

$$= 1 - \sqrt{1 - \frac{6m}{r} + \frac{m'r}{m}} \quad (46)$$

$$= 1 - \sqrt{1 + 3\left(\zeta - \frac{2m}{r}\right)}, \quad (47)$$

where ζ is the ratio of ϵ to the average mass density $\bar{\epsilon}(r)$ inside radius r ,

$$\zeta(r) = \frac{\epsilon}{\bar{\epsilon}} = \frac{m'r}{3m}, \quad (48)$$

$$\bar{\epsilon}(r) = \frac{3m}{4\pi r^3}. \quad (49)$$

The ratio ζ indicates the local-density effect of matters, which negatively contributes to ν . In contrast, the ratio $2m/r$ indicates how close r is to the gravitational radius $2m$ for the mass inside r and can be regarded as the general-relativistic effect, which positively contributes to ν . We should note that ν contains m and m' but not α . The form of ν implies that

$$0 < \nu < 1 \quad \text{for} \quad \zeta < \frac{2m}{r} < \zeta + \frac{1}{3}, \quad (50)$$

$$\nu = 0 \quad \text{for} \quad \zeta = \frac{2m}{r}, \quad (51)$$

$$\nu < 0 \quad \text{for} \quad \zeta > \frac{2m}{r}. \quad (52)$$

Hence, if the general-relativistic effect is larger than the local-density effect, the periapsis shift is prograde, whereas if it is smaller, the shift is retrograde.

IV. PERIAPSIS SHIFTS IN SPECIFIC MODELS

We parametrize the density profile of the Einstein cluster as (see, e.g., Ref. [38])

$$\epsilon(r) = \epsilon_* (r/d)^{-\gamma} [1 + (r/d)^\alpha]^{(\gamma-\beta)/\alpha} \Theta(r - r_{\min})\Theta(r_{\max} - r), \quad (53)$$

where ϵ_* is a constant, and $\Theta(\cdot)$ is the step function. In the following subsections, we focus on three models: (A) the constant density model as a simple toy model corresponding to $(\alpha, \beta, \gamma) = (\alpha, 0, 0)$, where α is indefinite; (B) the singular isothermal sphere model as the simplest dark halo model corresponding to $(\alpha, \beta, \gamma) = (\alpha, 2, 2)$, where α is indefinite [33]; (C) the Navarro-Frenk-White (NFW) profile, the universal profile of the dark matter distribution predicted by numerical simulations, corresponding to $(\alpha, \beta, \gamma) = (1, 3, 1)$ [34]. The model parameters we use are summarized in Table I.

A. Constant density model

We consider the continuous mass function (15)–(17) with

$$m_* = M_0 + \frac{4\pi\epsilon_*}{3}(r^3 - r_{\min}^3), \quad (54)$$

		(A) Constant density model				(B) Isothermal sphere model					
(α, β, γ)		$(\alpha, 0, 0)$				$(\alpha, 2, 2)$					
model		C1	C2	C3	C4	I1	I2	I3	I4	I5	I6
M		2	1.2	2	1.2	2.2	2.2	2.2	1.2	2	2
r_{\min}		6	6	6	6	5.8	6	6.2	10	6	5
r_{\max}		≤ 30	≤ 30	30	30	≤ 30	≤ 30	≤ 30	≤ 30	10	30
Figure		2(a)	2(b)	3(a)–3(c)	3(d)–3(f)	4(a)	4(b)	4(c)	4(d)	5(a)–5(c)	5(d)–5(f)

		(C) NFW model							
(α, β, γ)		$(1, 3, 1)$							
model		N1	N2	N3	N4	N5	N6	N7	N8
M		2	2	2	1.2	1.2	1.2	2	2
r_{\min}		6	6	6	10	10	10	6	6
r_{\max}		≤ 30	≤ 30	≤ 30	≤ 30	≤ 30	≤ 30	30	30
d		20	9	6	100	25	5	20	6
Figure		6(a)	6(b)	6(c)	6(d)	6(e)	6(f)	7(a)–7(c)	7(d)–7(f)

TABLE I. Summary of model parameters of Einstein clusters in units where $M_0 = 1$. The label C refers to the constant density model, I to the isothermal sphere model, and N to the NFW model.

where ϵ_* is a constant given by

$$\epsilon_* = \frac{3}{4\pi} \frac{M - M_0}{r_{\max}^3 - r_{\min}^3}. \quad (55)$$

This mass distribution is produced by the rectangular-shaped energy density profile

$$\epsilon = \epsilon_* \Theta(r - r_{\min}) \Theta(r_{\max} - r). \quad (56)$$

Therefore, we call this model the constant density model. There is no analytical expression for α .

It is worthwhile to consider the innermost stable circular orbit (ISCO), which satisfies $V = 0$, $V' = 0$, and $V'' = 0$. Provided that the mass fraction of the cluster is sufficiently small, i.e., $\eta = (M - M_0)/M_0 \ll 1$, if the ISCO appears on the matter distribution, then the radius is given by

$$r = 6M_0 \left[1 - \frac{r_{\min}^3 + 432M_0^3 \eta}{r_{\max}^3 - r_{\min}^3} + O(\eta^2) \right]. \quad (57)$$

This means that the ISCO radius is smaller than $6M_0$ of the Schwarzschild, which is caused by the matter distribution.

We focus on the nearly circular bound orbits on the matter distribution. In this model, the two ratios $2m/r$ and $\zeta = \epsilon/\bar{\epsilon}$ are reduced to

$$\frac{2m}{r} = \frac{2M_0}{r} + \frac{2(M - M_0)(r^3 - r_{\min}^3)}{r(r_{\max}^3 - r_{\min}^3)}, \quad \zeta = \frac{(M - M_0)r^3}{(M - M_0)r^3 + M_0r_{\max}^3 - Mr_{\min}^3}. \quad (58)$$

Figure 2(a) shows the contour plots of ν on the matter distribution for model C1. If $r_{\max} < 9.524$, then $\nu < 0$. When r_{\max} is relatively small, ϵ_* is relatively large. In this situation, the local-density effect becomes dominant over the general-relativistic effect, and as a result, retrograde shifts are more likely to occur. On the other hand, if $r_{\max} > 9.524$, then the region of $\nu > 0$ appears near $r = r_{\min}$. When r_{\max} is relatively large, ϵ_* is relatively small. Therefore, the general-relativistic effect becomes dominant over the local-density effect, and as a result, prograde shifts are more likely to occur. Figure 2(b) shows the result for model C2. If $r_{\max} < 7.017$, then $\nu < 0$. If $7.770 < r_{\max} < 12.976$, then $\nu > 0$. If $7.017 < r_{\max} < 7.770$ and $r_{\max} > 12.976$, then $\nu > 0$ near $r = r_{\min}$ and $\nu < 0$ near $r = r_{\max}$. Compared to the case of Fig. 2(a), the region of $\nu > 0$ appears from a smaller r_{\max} . This implies that the local-density effect is weaker, and the general-relativistic effect tends to dominate in a wider parameter range.

We now focus on a situation where the total mass of the matter distribution is much smaller than the black hole mass, $\eta = (M - M_0)/M_0 \ll 1$. We also assume that the matter is distributed widely enough and far enough away from the black hole, $r_{\max}/M_0 \gg 1$ and $(r_{\max} - r_{\min})/M_0 \gg 1$. Then we can estimate the radius at which $\nu = 0$ as

$$r \simeq \left(\frac{2M_0 r_{\max}^3}{\eta} \right)^{1/4} \approx 480 \left(\frac{M_0}{4.0 \times 10^6 M_\odot} \right)^{1/4} \left(\frac{r_{\max}}{1.9 \times 10^3 \text{ au}} \right)^{3/4} \left(\frac{0.01}{\eta} \right)^{1/4} \text{ au}, \quad (59)$$

where M_\odot is the solar mass, and the typical values of M_0 and r_{\max} are chosen as the mass of Sgr A* and the apoapsis distance of S2/S0-2, respectively. The typical value 480 au is between the periapsis and apoapsis distances of S2/S0-2. Thus, we see that the general-relativistic effect can be canceled out by the local-density effect here, and the retrograde periapsis shift occurs outside this radius. It suggests that the local-density effect may compensate the general-relativistic effect even if the matter distribution has only a mass fraction of 1% relative to the black hole.

Figure 3 shows several bound orbits of stars moving in the matter distribution, corresponding Figs. 3(a)–3(c) to model C3, and Figs. 3(d)–3(f) to model C4. The solid curves denote the orbits of stars revolving counterclockwise in the x-y plane, where $(x, y) = (r \cos \varphi, r \sin \varphi)$. When a small amount of energy ΔE is injected to a star on a circular orbit, the orbit transits to a bound orbit of nearly circular shape [see Figs. 3(a) and 3(d)]. The amplitude of radial oscillation increases with ΔE [see Figs. 3(b) and 3(e)]. In Figs 3(c) and 3(f), each orbit extends across the entire matter

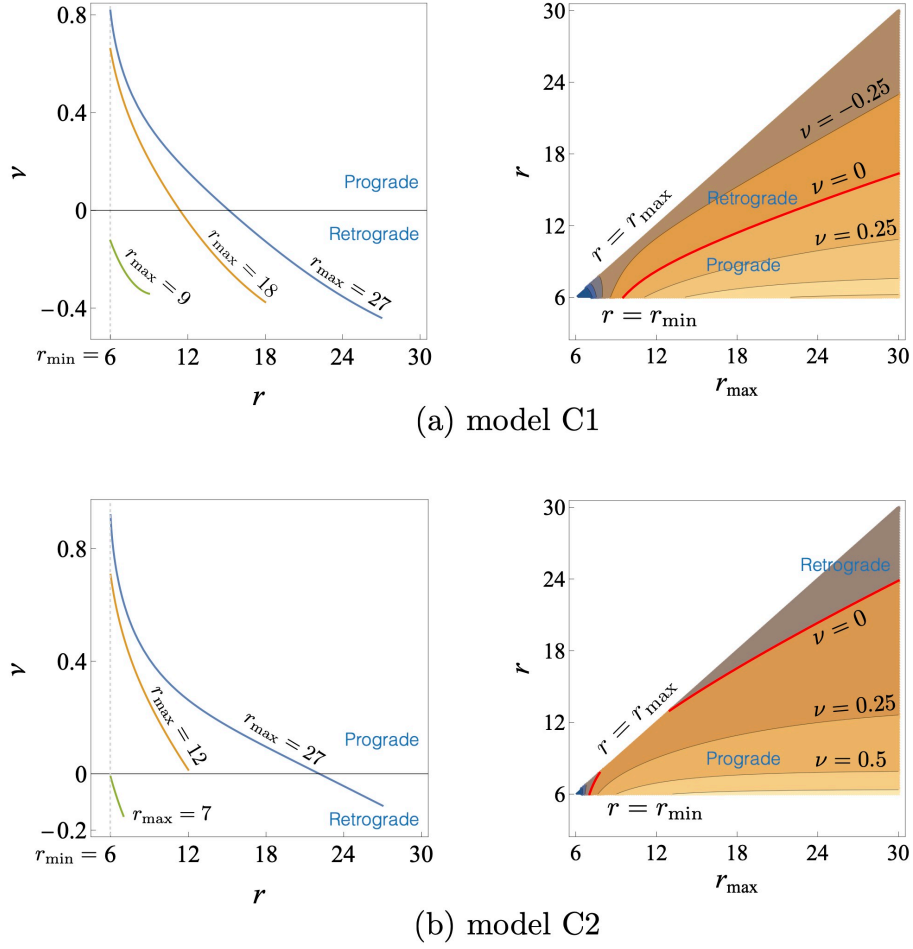


FIG. 2. Precession rate ν on the matter distribution for the constant density models C1 and C2. See Table I for the summary of the parameter values. The left panels show ν as a function of r for several fixed values of r_{\max} . The right panels show the contours of ν in the range $r_{\min} \leq r \leq r_{\max}$. The red solid curves denote $\nu = 0$.

distribution. The red and blue dots indicate the periapses and apoapses of the bound orbits, respectively. Figures 3(a)–3(c) show their retrograde shifts, where the blue and red dots revolve clockwise. On the other hand, Figs 3(d)–3(f) show their prograde shifts, where the blue and red dots revolve counterclockwise. We can see that even if the amplitude of the radial oscillation becomes large by injecting energy, the shift direction is the same as in the case of nearly circular bound orbits.

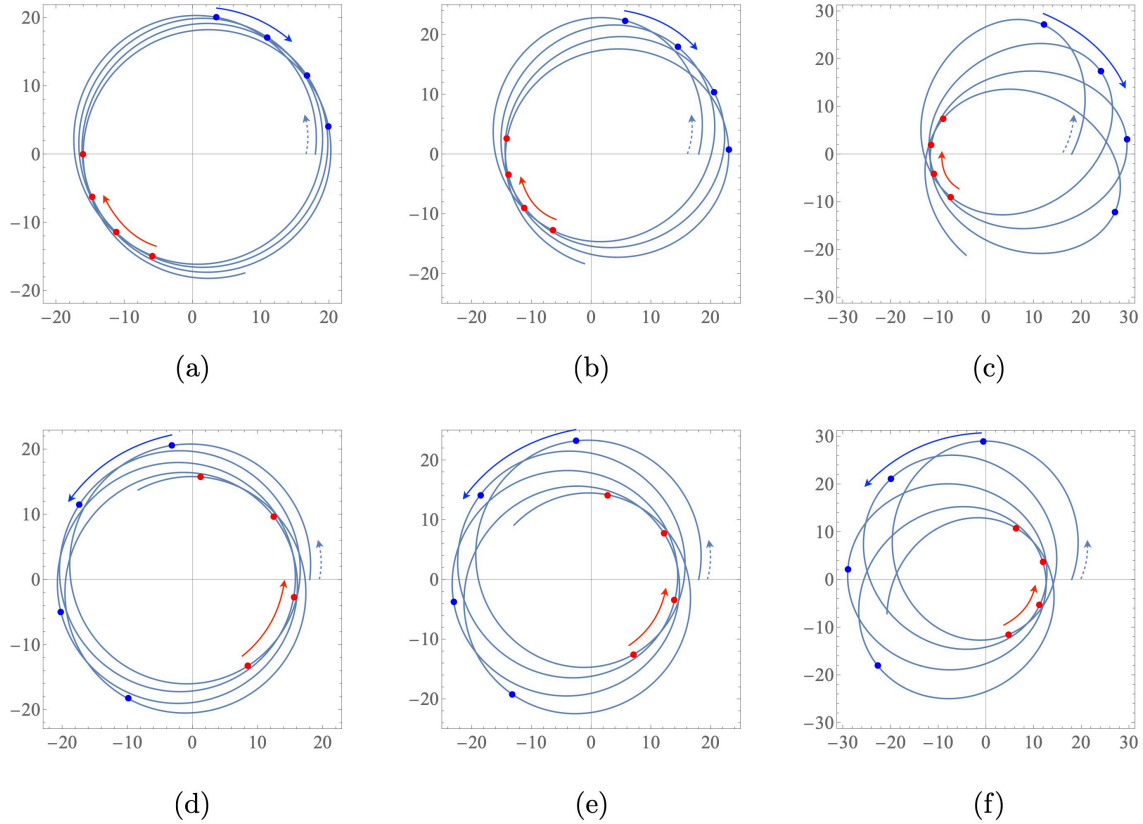


FIG. 3. Periaapsis (red dots) and apoapsis (blue dots) shift of bound orbits (solid curves) on the x - y plane in models C3 and C4, where $(x, y) = (r \cos \varphi, r \sin \varphi)$. See Table II for initial conditions.

Figure	3(a)	3(b)	3(c)	3(d)	3(e)	3(f)
$r(0)(= r_c)$	18	18	18	18	18	18
$\varphi(0)$	0	0	0	0	0	0
E	9.934223e-1	9.3627e-1	9.445e-1	9.27945e-1	9.2896e-1	9.3199e-1
$E - E(r_c)$	6.82e-4	2.73e-3	1.09e-2	5.05e-4	1.52e-3	4.55e-3
$L(= L(r_c))$	5.222	5.222	5.222	5.222	5.222	5.222
halo model	C3	C3	C3	C4	C4	C4

TABLE II. Initial conditions of particle orbits in constant density models in units and the gauge where $M_0 = 1$ and $C = 1$. The values of $\dot{r}(0)$ are determined from Eq. (36).

B. Isothermal sphere model

We consider the continuous mass function (15)–(17) with

$$m_* = \sigma r + \delta, \quad (60)$$

where

$$\sigma = \frac{M - M_0}{r_{\max} - r_{\min}}, \quad (61)$$

$$\delta = \frac{M_0 r_{\max} - M r_{\min}}{r_{\max} - r_{\min}}. \quad (62)$$

The mass distribution m_* is produced by the density profile of the truncated singular isothermal sphere,

$$\epsilon = \frac{\sigma}{4\pi r^2} \Theta(r - r_{\min}) \Theta(r_{\max} - r). \quad (63)$$

Therefore, we call this model the isothermal sphere model. If $\sigma \neq 1/2$, the corresponding α is given by Eqs. (21)–(23) with

$$\alpha_* = \frac{r}{2} - \frac{C_*^2}{2} (r - 2m_*)^{1/(1-2\sigma)}, \quad (64)$$

where C_* is an integral constant giving the shift degree of freedom of the time coordinate. The boundary conditions (24) and (25) give the relations,

$$C_0 = C_* (r_{\min} - 2M_0)^{\sigma/(1-2\sigma)}, \quad (65)$$

$$C = C_* (r_{\max} - 2M)^{\sigma/(1-2\sigma)}. \quad (66)$$

If $\sigma = 1/2$, the corresponding α_* takes the form

$$\alpha_* = \frac{r}{2} - \frac{C_*^2}{2} e^{r/(r_{\min} - 2M_0)}, \quad (67)$$

where C_* is an integration constant giving the shift degree of freedom of the time coordinate. The boundary conditions (24) and (25) lead to

$$C_0 = C_* \frac{e^{r_{\min}/2(r_{\min} - 2M_0)}}{\sqrt{r_{\min} - 2M_0}}, \quad (68)$$

$$C = C_* \frac{e^{r_{\max}/2(r_{\max} - 2M)}}{\sqrt{r_{\max} - 2M}}. \quad (69)$$

For $\eta = (M - M_0)/M_0 \ll 1$, if the ISCO appears on the matter distribution, its radius is given by

$$r = 6M_0 \left[1 - \frac{r_{\min}}{r_{\max} - r_{\min}} \eta + O(\eta^2) \right]. \quad (70)$$

This means that the ISCO is smaller than $6M_0$ of the Schwarzschild, which is caused by the matter distribution.

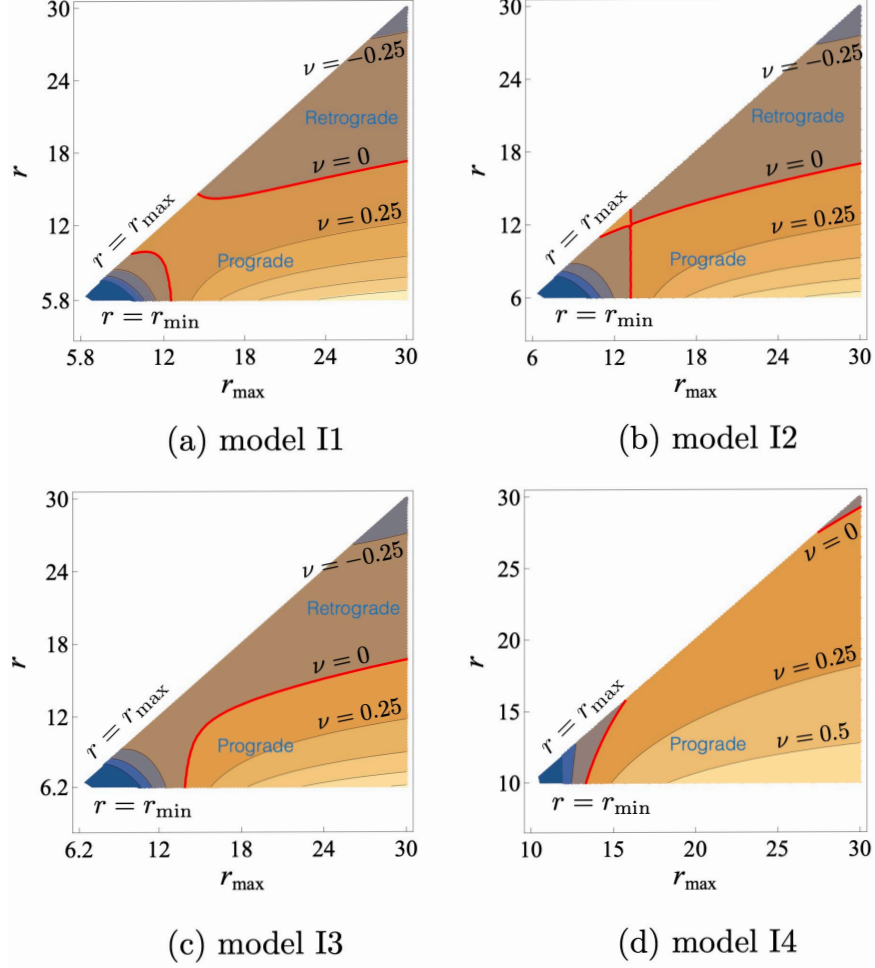


FIG. 4. Contours of ν (0.25 intervals) in models I1–I4. See Table I for the summary of the parameter values. The red solid curves denote $\nu = 0$.

We focus on the nearly circular bound orbits on the matter distribution. The two ratios $2m/r$ and ζ of this model are reduced to

$$\frac{2m}{r} = 2\sigma + \frac{2\delta}{r}, \quad \zeta = \frac{\sigma r}{3(\sigma r + \delta)}. \quad (71)$$

Figure 4(a) shows the contour plots of ν on the matter distribution in model I1. If $r_{\max} < 9.640$, then $\nu < 0$; if $12.528 < r_{\max} < 14.559$, then $\nu > 0$; if $r_{\max} > 14.559$, then $\nu > 0$ near $r = r_{\min}$ and $\nu < 0$ near $r = r_{\max}$. These behaviors can be interpreted in the same way as the constant density model. However, there is a novel situation, where $\nu < 0$ near $r = r_{\min}$ and $\nu > 0$ near $r = r_{\max}$ in $9.640 < r_{\max} < 12.528$, which is not found in the constant density model (see Fig. 2). Since the local density is proportional to r^{-2} , we can see that the local-density effect in this range decreases to such an extent that the general-relativistic effect dominates as r increases. In Fig. 4(b), the contour of $\nu = 0$ makes a vertical segment at $r_{\max} = 13.2$, where $\nu = 0$ appears in the whole range

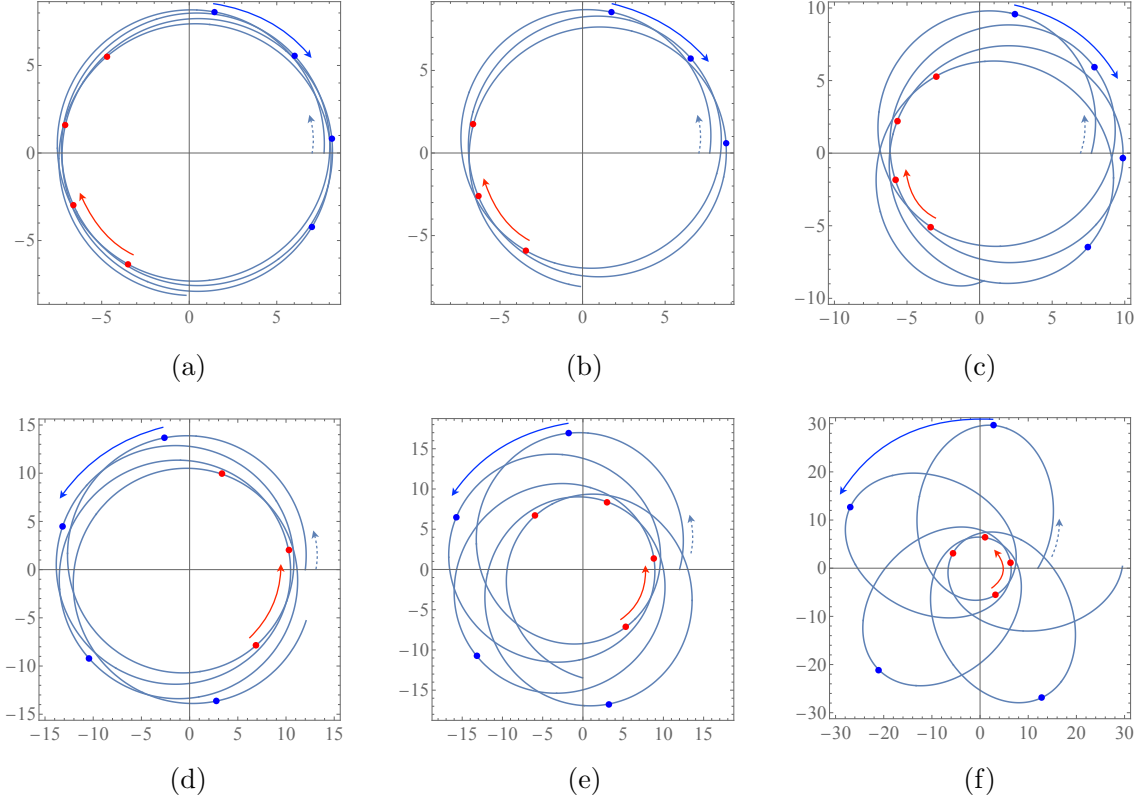


FIG. 5. Periapsis (red dots) and apoapsis (blue dots) shift of bound orbits (solid curves) on the x-y plane in models I5 and I6. See Table III for initial conditions.

of r . This is a special case unique to the isothermal sphere model. In Fig. 4(c), the plot shows qualitatively the same behavior as the case in Fig. 2(a). Figures 4(a)–4(c) show the change of the contours as the value of r_{\min} gradually increases. Figure 4(d) is the case of model I4 and shows qualitatively the same behavior as the case in Fig. 2(b).

We now focus on a situation where $\eta \ll 1$. We also assume that $r_{\max}/M_0 \gg 1$ and $(r_{\max} - r_{\min})/M_0 \gg 1$. Then we can estimate the radius at which $\nu = 0$ as

$$r \simeq \left(\frac{6r_{\max}M_0}{\eta} \right)^{1/2} \approx 210 \left(\frac{r_{\max}}{1.9 \times 10^3 \text{ au}} \right)^{1/2} \left(\frac{M_0}{4.0 \times 10^6 M_\odot} \right)^{1/2} \left(\frac{0.01}{\eta} \right)^{1/2} \text{ au}, \quad (72)$$

where the typical values are chosen as the same as in the previous subsection. The typical value 210 au is comparable to the periapsis distance 120 au of S2/S0-2. As in the previous model, it is suggested that the local-density effect cancels out the general-relativistic effect even if the matter distribution has only a 1% mass fraction relative to the black hole.

Figures 5(a)–5(c) show particle orbits in model I5. We see that the retrograde periapsis shift occurs. Figures 5(d)–5(f) show the case of model I6. When the energy slightly increases from that of the circular orbit, the orbital shape becomes quasi-circular [see Fig. 5(d)]. As the energy

Figure	5(a)	5(b)	5(c)	5(d)	5(e)	5(f)
$r(0)$	7.7	7.7	7.7	12	12	12
$\varphi(0)$	0	0	0	0	0	0
E	8.50007e-1	8.5271e-1	8.635e-1	9.1452e-1	9.1921e-1	9.427e-1
$E - E(r_c)$	9.02e-4	3.61e-3	1.44e-2	1.17e-3	5.87e-3	2.93e-2
$L(= L(r_c))$	4.967	4.967	4.967	4.753	4.753	4.753
halo model	I5	I5	I5	I6	I6	I6

TABLE III. Initial conditions of particle orbits in isothermal sphere models in units and the gauge where $M_0 = 1$ and $C = 1$. The values of $\dot{r}(0)$ are determined from Eq. (36).

increases, the radial amplitude increases [see Figs. 5(e) and 5(f)]. These cases show the prograde periapsis shifts. We can see that even if the amplitude of the radial oscillation becomes large by injecting energy, the shift direction is the same as in the quasi-circular case.

C. NFW model

We consider the continuous mass function (15)–(17) with

$$m_* = M_0 + 4\pi\epsilon_s d^3 \left[\ln \left(\frac{1+r/d}{1+r_{\min}/d} \right) + \frac{1}{1+r/d} - \frac{1}{1+r_{\min}/d} \right], \quad (73)$$

where d is a constant called the scale radius, and ϵ_* is a constant given by

$$\epsilon_* = \frac{M - M_0}{4\pi d^3} \left[\ln \left(\frac{1+r_{\max}/d}{1+r_{\min}/d} \right) + \frac{1}{1+r_{\max}/d} - \frac{1}{1+r_{\min}/d} \right]^{-1}. \quad (74)$$

The mass distribution m_* is produced by the Navarro-Frenk-White (NFW) profile [34]

$$\epsilon = \frac{\epsilon_*}{(r/d)(1+r/d)^2} \Theta(r - r_{\min}) \Theta(r_{\max} - r). \quad (75)$$

Therefore, we call this model the NFW model.

For $\eta \ll 1$, if the ISCO appears on the matter distribution, its radius is given by

$$r = 6M_0 \left[1 - \frac{1 - \ln(6M_0/r_{\min})}{\ln(r_{\max}/r_{\min})} \eta + O(\eta^2) \right] \quad (76)$$

in the limit $d \rightarrow 0$, and

$$r = 6M_0 \left[1 - \frac{r_{\min}^2 + 36M_0^2}{r_{\max}^2 - r_{\min}^2} \eta + O(\eta^2) \right] \quad (77)$$

in the limit $d/M_0 \rightarrow \infty$. These values are smaller than $6M_0$ of the Schwarzschild, which is caused by the matter distribution.

Figure	7(a)	7(b)	7(c)	7(d)	7(e)	7(f)
$r(0)(= r_c)$	18	18	18	18	18	18
$\varphi(0)$	0	0	0	0	0	0
E	9.3913e-1	9.4149e-1	9.486e-1	9.4332e-1	9.4569e-1	9.528e-1
$E - E(r_c)$	1.18e-3	3.55e-3	1.06e-2	1.18e-3	3.55e-3	1.06e-2
$L(= L(r_c))$	5.946	5.946	5.946	5.946	5.946	5.946
halo model	N7	N7	N7	N8	N8	N8

TABLE IV. Initial conditions of particle orbits in NFW models in units and the gauge where $M_0 = 1$ and $C = 1$. The values of $\dot{r}(0)$ are determined from Eq. (36).

Figures 6(a)–6(f) show the contour plots of ν on the matter distribution in models N1–N6, respectively. Figures 6(a) and 6(d) show qualitatively the same behaviors as in Figs. 2(a) and 4(c). Figure 6(c) shows qualitatively the same behavior as in Fig. 4(a). Figures 6(e) and 6(f) show qualitatively the same behaviors as in Figs. 2(b) and 4(d). Consider Fig. 6(b), which shows a novel $\nu = 0$ behavior that has not appeared in the previous cases. If $r_{\max} < 11.290$, then $\nu < 0$; if $12.217 < \nu < 15.324$, then $\nu > 0$; if $\nu > 15.324$, then $\nu < 0$ near $r = r_{\max}$ and $\nu > 0$ near $r = r_{\min}$. These behaviors can be interpreted in the same way as the constant density model and the isothermal sphere model. If $11.290 < r_{\max} < 11.814$, then $\nu < 0$ near $r = r_{\min}$ and $\nu > 0$ near $r = r_{\max}$. The same behavior is seen in the case of Fig. 4(a) of the isothermal sphere model. If $11.814 < r_{\max} < 12.217$, then $\nu > 0$ near $r = r_{\min}$ and $r = r_{\max}$, whereas $\nu < 0$ in the intermediate region, where d is comparable to the distribution scale. This behavior is not seen in the previous two models.

Assume that $M_0 = 4.0 \times 10^6 M_\odot$, $\eta = 0.01$, $r_{\max} = 1.9 \times 10^3$ au, and $r_{\min} = 1.2 \times 10^2$ au. Then we can estimate the radius at which $\nu = 0$ as $r \approx 130$ au for $d \approx 0$, $r \approx 200$ au for $d = 100$ au, and $r \approx 420$ au for $d = 1 \times 10^4$ au. As in the previous two cases, the local-density effect can compensate for the general-relativistic effect in a realistic observational range, even if the mass fraction is 1%.

Figure 7 shows several bound orbits on the matter distribution in models N7 and N8. As $E - E(r_c)$ increases from (a) to (c) or from (d) to (f), the amplitude of the radial oscillation increases. The first line shows retrograde periapsis shifts, while the second line shows prograde periapsis shifts.

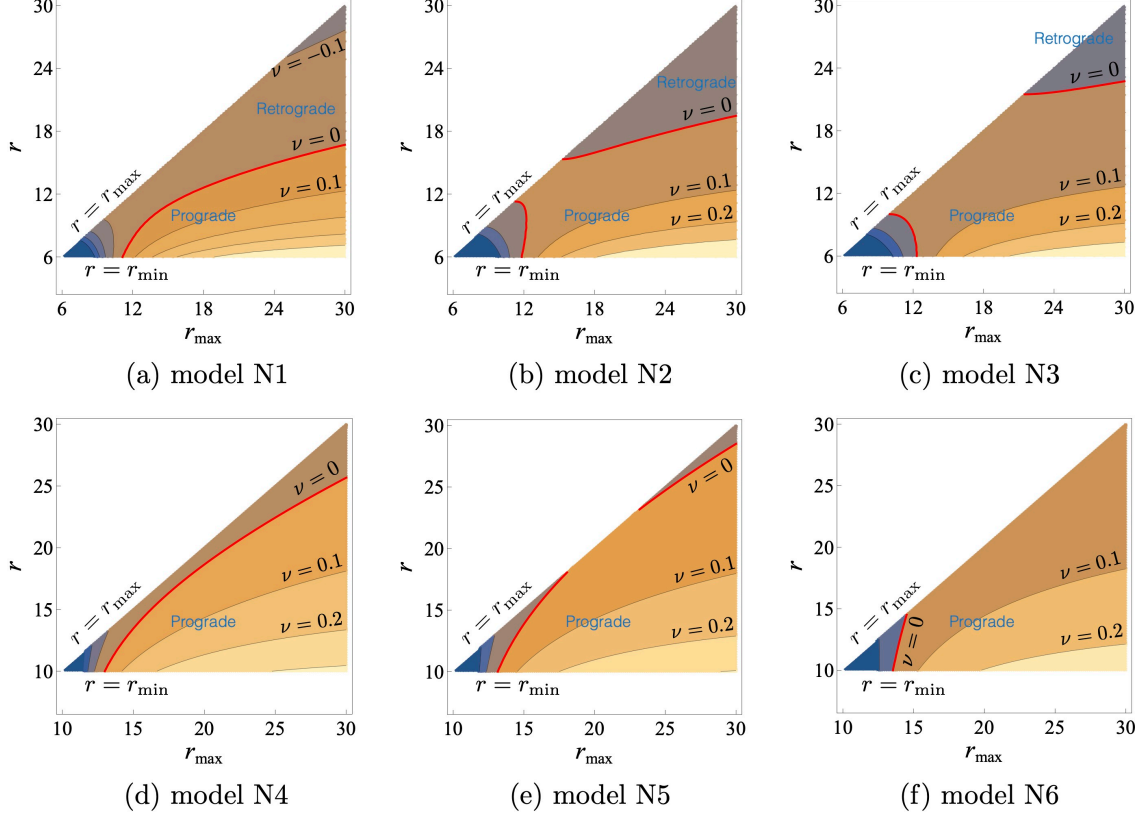


FIG. 6. Contour plots of the precession rate ν for models N1–N6. See Table I for the summary of the parameter values. The red curves denote $\nu = 0$. The contour interval is 0.1.

V. MODEL FUNCTIONS AND OBSERVABLES

We consider whether the model functions $m(r)$, $\alpha(r)$, and $\epsilon(r)$ are determined by observations of photons coming from orbiting stars. Assume that a distant observer observes a nearly circular bound orbit from its orbital axis (i.e., face on to the orbital plane). Then we focus on the following four observables: The orbital period T_φ , the periapsis shift angle $\Delta\varphi_p$ of the nearly circular bound orbit, the redshift factor z of photons coming from the star (the so-called spectroscopic observable), and the angular radius β of the orbital radius of the star on the celestial sphere. The two observables T_φ and $\Delta\varphi_p$ can be measured by continuous observation at least for one orbital period. In the present spacetime, using Eqs. (32), (40), (43), and (44), these observables are represented as

$$T_\varphi = \frac{2\pi}{d\varphi/dT} = 2\pi \sqrt{\left. \frac{r^3 r - 2m}{m r - 2\alpha} \right|_s}, \quad (78)$$

$$\Delta\varphi_p = \frac{2\pi}{\omega_r} (\omega_\varphi - \omega_r) = 2\pi \frac{\nu}{1 - \nu} = 2\pi \left[\left(1 + \frac{4\pi r^3 \epsilon}{m} - \frac{6m}{r} \right)^{-1/2} - 1 \right]_s, \quad (79)$$

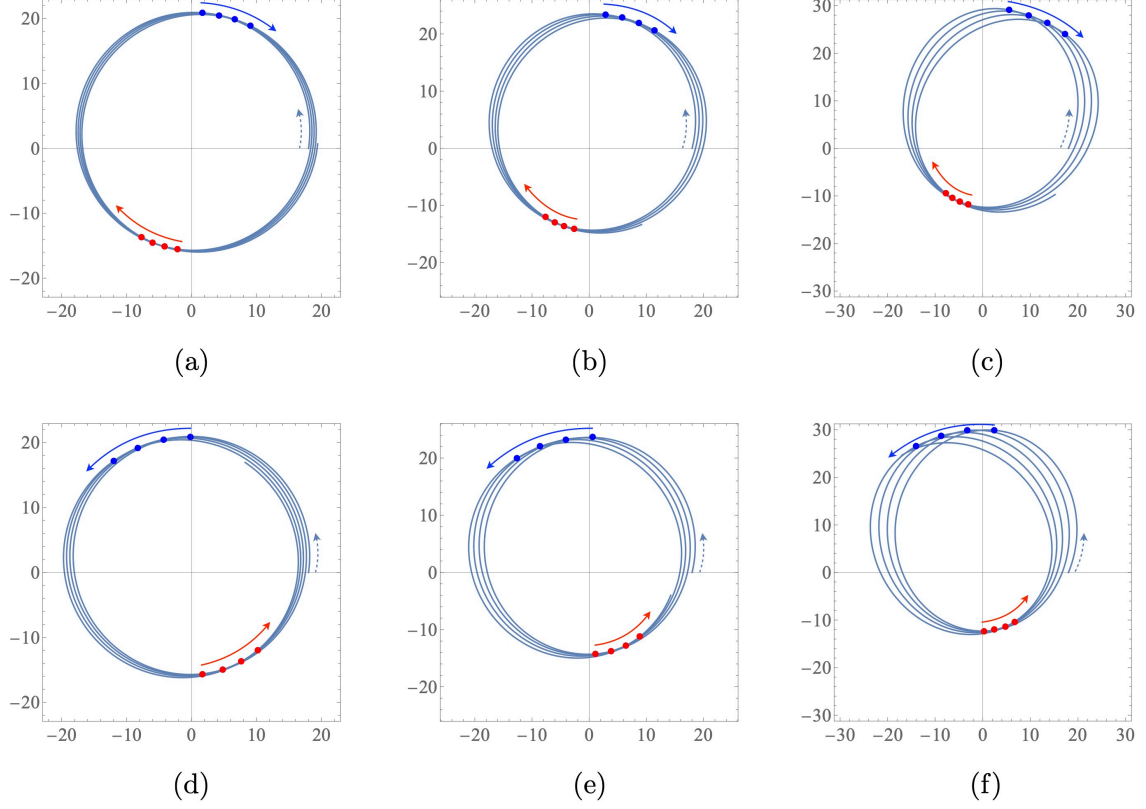


FIG. 7. Bound orbits and their periastron and apastron shifts in models N7 and N8. The curves and dots are defined in the same way as in Fig. 3. See Table IV for initial conditions.

where $d\varphi/dT = (d\varphi/dt)(dt/dT) = C^{-1}\dot{\varphi}/\dot{t}$, we have chosen $C = 1$, and the symbol “s” means the quantities for the source. The others, z and β , are given by the momentum k_μ of photons coming from the star,

$$1 + z = \frac{(k_\mu u_s^\mu)|_s}{(k_\mu u_o^\mu)|_o} = \dot{t} - b\dot{\varphi}, \quad (80)$$

$$\sin \beta = \sqrt{(k^{(2)}/k^{(0)})^2 + (k^{(3)}/k^{(0)})^2} \Big|_o = \frac{q}{r_o} \sqrt{1 - \frac{2\alpha(r_o)}{r_o}}, \quad (81)$$

where the symbol “o” means the quantities for the observer, and b and q are constants of photon motion known as the impact parameters,

$$b = \frac{k_\varphi}{(-k_t)}, \quad (82)$$

$$q = \frac{1}{(-k_t)} \sqrt{k_\theta^2 + \frac{k_\varphi^2}{\sin^2 \theta}}, \quad (83)$$

and $u_s^\mu = (\dot{t}, 0, 0, \dot{\varphi})$ and $u_o^\mu = (1, 0, 0, 0)$ are the velocity of the star and that of the distant observer in the coordinates (t, r, θ, φ) , respectively, and $k^{(\mu)}$ is the tetrad components of k_μ (see Appendix B

for details). Using the assumption of the observer being face-on, we can set $b = 0$ by the coordinate transformation, and then

$$1 + z = \sqrt{\frac{r}{r-3m} \frac{r-2m}{r-2\alpha}} \Big|_s, \quad (84)$$

where we have used Eqs. (32) and (40). Furthermore, in the face-on case, because only the photons with zero radial velocity at the emission point will reach the distant observer on the axis, the parameter q takes the value

$$q^2 = \frac{r^3}{r-2\alpha} \Big|_s, \quad (85)$$

where we have used the radial equation for photon motion,

$$\left(\frac{dr}{d\lambda}\right)^2 + \left(1 - \frac{2m}{r}\right) \left(\frac{q^2}{r^2} - \frac{r}{r-2\alpha}\right) = 0, \quad (86)$$

where λ is an affine parameter. Using $r_o \gg M$ and $\beta \ll 1$, we obtain

$$\beta = \frac{r_s}{r_o \sqrt{1 - 2\alpha(r_s)/r_s}}. \quad (87)$$

If we know the value of r_o , by measuring the four observables $\Delta\varphi_p$, T_φ , z , and β for a nearly circular bound orbit in the face-on case, we obtain the values of $m(r_s)$, $\alpha(r_s)$, $\epsilon(r_s)$, and the equilibrium radius r_s . Therefore, by using observational data for several stars orbiting at different radii, we can obtain the functions of our model by appropriate interpolation. In contrast, if we do not know the value of r_o , we obtain a relationship between two sets of dimensionless quantities ($\Delta\varphi_p$, T_φ/r_s , z , β) and ($m(r_s)/r_s$, $\alpha(r_s)/r_s$, $\epsilon(r_s)r_s^2$, and r_o/r_s). Note that, however, for the observer not in the face-on to the nearly circular orbital plane of the star, the situation becomes much more convoluted due to the uncertainties in measuring the values of the orbital shift angle $\Delta\varphi_p$ and the the position on the celestial sphere (X, Y) (see Appendix B).²

To make the discussion clear, we focus for a while on a quasi-Newtonian nearly circular quasi-elliptical orbit with an equilibrium radius r_s , where $r_s \gg m(r_s)$, $r_s \gg \alpha(r_s)$, and $|\nu| \ll 1$. In this case, the periapsis shift $\Delta\varphi_p$ is given by the following simple formula:

$$\Delta\varphi_p = 3\pi \left(\frac{2m}{r} - \frac{\epsilon}{\bar{\epsilon}} \right) \Big|_s. \quad (88)$$

² These uncertainties arise from the gravitational lens effect on the orbit of photons coming from the source to the observer. For $\Delta\varphi_p$, the gravitational lens effect deforms the visible shape of the star orbit, and the exact value of $\Delta\varphi_p$ cannot be measured from the shape without prior knowledge of the metric functions $m(r)$ and $\alpha(r)$. For (X, Y) , although they are related to $(q, b/\sin\theta_o)$ through Eqs. (B6) and (B7), neither the relation $b = 0$ nor Eq. (85) is valid in general because of the lens effect. However, if the deviation from the face-on case is small, or equivalently, if the inclination angle is small (i.e., $i = \theta_0 \ll 1$), the discussion for the face-on case holds approximately. Then the correction is typically given by the projection of the line-of-sight direction to the face-on direction, whose order is expected to be $O(1 - \cos i) = O(i^2)$.

Then we derive the concrete expressions for $m(r_s)$, $\alpha(r_s)$, and $\epsilon(r_s)$ and therefore the deviation from the Schwarzschild solution. For such an orbit, we can determine the mass m_s , the radius r_s , and the inclination angle $i = \theta_o$ using the maximum and minimum separations from the central object, $r_s = r_o \max(\beta)$ and $r_s \cos i = r_o \min(\beta)$, respectively; the orbital period, $T_\varphi = 2\pi\sqrt{r^3/m}|_s$; and the difference between the maximum and minimum redshifts,

$$\max(z) - \min(z) = 2\sqrt{m/r}|_s \sin i. \quad (89)$$

Then, if the periapsis shift angle $\Delta\varphi_p$ is observed, the values of the functions $\epsilon/\bar{\epsilon}$ and α at the source are obtained by

$$\frac{\epsilon}{\bar{\epsilon}}\Big|_s = -\frac{\Delta\varphi_p}{3\pi} + \frac{2m}{r}\Big|_s, \quad (90)$$

$$\alpha(r_s) = r_s \langle z \rangle - \frac{m(r_s)}{2}, \quad (91)$$

where $\langle z \rangle$ is the redshift of the star averaged over one orbital period, and we have used Eq. (84) to obtain Eq. (91). We can recast the above equations to the following form:

$$\epsilon(r_s) = \frac{3m^2}{2\pi r^4}\Big|_s \frac{\Delta\varphi_{p,\text{conv}} - \Delta\varphi_p}{\Delta\varphi_{p,\text{conv}}}, \quad (92)$$

$$\frac{\alpha - m}{m}\Big|_s = \frac{3}{2} \frac{\langle z \rangle - \langle z \rangle_{\text{conv}}}{\langle z \rangle_{\text{conv}}}, \quad (93)$$

where the symbol ‘‘conv’’ stands for conventional, and $\Delta\varphi_{p,\text{conv}}$ and $\langle z \rangle_{\text{conv}}$ are the conventional expressions for $\Delta\varphi_p$ and $\langle z \rangle$, respectively,

$$\Delta\varphi_{p,\text{conv}} = \frac{6\pi m}{r}\Big|_s, \quad (94)$$

$$\langle z \rangle_{\text{conv}} = \frac{3m}{2r}\Big|_s. \quad (95)$$

Thus, if we know the value of r_o , we can *locally* determine not only the deviation of $\alpha(r_s)$ from the gravitational mass $m(r_s)$ but also the energy density $\epsilon(r_s)$ at the orbital radius of the star. The accuracy in observing $\langle z \rangle$ determines the sensitivity to the deviation $\alpha(r_s)$ from $m(r_s)$, while the accuracy in observing $\Delta\varphi_p$ determines the sensitivity to ϵ . If we normalize the parameters by typical values for S2/S0-2 near Sgr A*, we obtain for the latter

$$\epsilon(r_s) \approx 3.7 \times 10^{-5} M_\odot \text{ au}^{-3} \left(\frac{\Delta\varphi_{p,\text{conv}} - \Delta\varphi_p}{\Delta\varphi_{p,\text{conv}}} / 0.1 \right) \left(\frac{m}{4.0 \times 10^6 M_\odot} \right)^2 \left(\frac{r_s}{120 \text{ au}} \right)^{-4}, \quad (96)$$

where $\Delta\varphi_{p,\text{conv}} \approx 0.36^\circ [m/(4.0 \times 10^6 M_\odot)](r_s/120 \text{ au})^{-1}$. If we can implement the above analysis for many stars of different r_s , we can check whether such obtained functions $\alpha(r)$, $m(r)$, and $\epsilon(r)$ satisfy Eqs. (5) and (7) and thus check the Einstein cluster solution as a model of the gravitational field sourced by dark matter particles surrounding the central black hole.

VI. SUMMARY AND DISCUSSION

We have considered the periapsis shift of geodesic bound orbits on physically reasonable static clouds in an asymptotically flat black hole spacetime. We ensure that the background spacetime constructed as the Schwarzschild black hole surrounded by a static Einstein cluster satisfies the four energy conditions (i.e., the weak, strong, null, and dominant energy conditions) in the entire region. In the framework of general relativity, we have explored how matter distribution affects the prograde shift of an orbiting star (the periapsis shift in the same direction as the revolution) observed in vacuum black hole spacetimes. Consequently, we have shown that the precession rate ν of the nearly circular bound orbits is determined by the relative magnitude of the following two terms of the opposite signs: The ratio of the gravitational radius for the gravitational mass contained within the equilibrium orbital radius to its equilibrium radius, $2m/r$, with a positive sign and the ratio of the local energy density to the averaged energy density within the equilibrium radius, $\zeta = \epsilon/\bar{\epsilon}$, with a negative sign. If the general-relativistic effect dominates over the local-density effect (i.e., $2m/r > \zeta$), then the prograde shift occurs (i.e., $0 < \nu < 1$), while if the local-density effect dominates over the general-relativistic effect (i.e., $\zeta > 2m/r$), then the retrograde shift occurs (i.e., $\nu < 0$). This result means that the negative contribution to the periapsis shifts naturally appears as a consequence of the extended distribution of physically reasonable matters even in general relativity. Note that even though a retrograde shift occurs, it does not imply any exotic spacetime (e.g., naked-singular spacetimes or wormhole spacetimes) but simply the existence of significant local energy density on the orbit of the star. Furthermore, if the prograde shift exceeds the value expected from the general-relativistic effect, it implies that the local energy density is negative, thus violating the energy conditions.

We have revealed that, if the distance from the observer to the star is given, the four quantities for a nearly circular bound orbit (i.e., the orbital shift angle, the radial oscillation period, the redshift, and the source position mapped onto the observer's sky) determine the local values of the background model functions. Therefore, the model functions can be extrapolated by measuring such observables with different radii. A notable advantage of focusing on nearly circular bound orbits is that the shape of the model functions can be estimated without assuming a concrete functional form. The discussion is much clearer for quasi-circular orbits in the post-Newtonian regime.

Furthermore, we have estimated the precession rate of nearly circular bound orbits in the constant density model, the isothermal sphere model, and the NFW model. A common property

of these models is that if the matter distribution is sufficiently broadened while the total mass is fixed, the prograde periapsis shift occurs due to the dominant general-relativistic effect near the inner boundary of the distribution. Conversely, the retrograde shift occurs due to the dominant local-density effects near the outer boundary of the distribution. In the situation at the center of our galaxy, we find that even if the mass fraction of the matter to the black hole is only 1% [36, 37], the local-density effect can compensate for the prograde shift due to the general-relativistic effect, which is consistent with the result in Ref. [12]. Furthermore, if the matter distribution is localized in a narrow region while the total mass is fixed, the local-density effect tends to dominate over the general-relativistic effect, so that the retrograde shift occurs. In the intermediate situation, there appears a variety of behaviors depending on the density distribution. Thus, we can extract information about the matter distribution from the distribution of the periapsis shifts.

We have also numerically simulated several bound orbits with large eccentricity on the matter distribution. In the parameter range explored in this study, the shift direction remains unchanged even when a nearly circular bound orbit transits to a bound orbit with large eccentricity by injecting energy. It suggests that the onset of prograde and retrograde periapsis shifts revealed by nearly circular elliptical orbits is also approximately valid even for bound orbits with large eccentricity.

This study uses a static and spherically symmetric black hole spacetime surrounded by a self-gravitating cluster of massive particles to consider the competing effects, the general-relativistic one and the local-density one on the periapsis shifts. However, several future projects (e.g., Thirty Meter Telescope) are expected to achieve the accuracy to measure even the frame-dragging effect of Sgr A* from the observations of S-stars. Therefore, it is an interesting future issue to clarify the competition between the spin effects and the local-density effects for phenomena such as periapsis shifts near a rotating black hole.

Though this study has concerned the effect of local matter density distribution on the dynamics of stars, the effect of matter distribution on the light rays or photon orbits is another interesting issue. We will report in a separate paper on the effect of matter distribution on phenomena such as gravitational lensing, a photon sphere, and gravitational redshifts in a black hole spacetime with static clouds.

Appendix A: Derivation of the stress-energy tensor for the Einstein cluster

We review the derivation of the stress-energy tensor for the Einstein cluster according to Einstein [17]. Assume that the matter field consists of a cluster of many freely falling particles with

equal mass m_p . This means that each particle moves according to the Lagrangian (31) with m_p restored. Then the momentum of each particle is $p_\mu = m_p g_{\mu\nu} \dot{x}^\nu$ and must satisfy $p_\mu p^\mu = -m_p^2$. This constraint equation can be separated into two equations via the separation constant L_p as

$$\left(1 - \frac{2m}{r}\right)^2 p_r^2 + \left(1 - \frac{2m}{r}\right) \left(\frac{L_p^2}{r^2} + m_p^2\right) = \frac{r-2m}{r-2\alpha} \mathcal{E}_p^2, \quad (\text{A1})$$

$$L_p^2 = p_\theta^2 + \frac{p_\varphi^2}{\sin^2 \theta}, \quad (\text{A2})$$

where $\mathcal{E}_p = -p_t$ is the conserved energy and $L_p \geq 0$ is the total angular momentum. Each particle of the Einstein cluster moves on a circular orbit. Therefore, L_p and \mathcal{E}_p are written as functions of the orbital radius r , as shown in Eqs. (39) and (40),

$$\frac{L_p^2}{m_p^2} = \frac{mr^2}{r-3m}, \quad (\text{A3})$$

$$\frac{\mathcal{E}_p^2}{m_p^2} = \left(1 - \frac{2\alpha}{r}\right) \frac{r-2m}{r-3m}. \quad (\text{A4})$$

We now focus on the particles in circular motion passing through a spacetime point x . Such particles have the same value of L_p because they are in the same spherical layer. However, the pair of specific momentum components p_θ/L_p and $p_\varphi/(L_p \sin \theta)$ can be distributed on the unit circle, as seen from Eq. (A2). Thus, we can parametrize these components by a variable ξ ($0 \leq \xi \leq 2\pi$) as

$$\left(\frac{p_\theta(x; \xi)}{L_p}, \frac{p_\varphi(x; \xi)}{L_p \sin \theta}\right) = (\cos \xi, \sin \xi). \quad (\text{A5})$$

We evaluate the stress-energy tensor $T_{\mu\nu}(x)$ by averaging over randomly distributed momentum in the phase space. Suppose that $T^\mu{}_\nu(x)$ takes the following form:

$$T^\mu{}_\nu(x) = \frac{n(r)}{m_p} \langle p^\mu p_\nu \rangle, \quad (\text{A6})$$

where $n(r)$ is the proper number density, and $\langle \cdot \rangle$ denotes averaging over all possible orbits passing through a point x . By formulating the averaging in terms of ξ , we can calculate Eq. (A6) for the Einstein cluster as

$$T^\mu{}_\nu(x) = \frac{n}{m_p} \frac{1}{2\pi} \int_0^{2\pi} p^\mu(x; \xi) p_\nu(x; \xi) d\xi = \text{diag}(-\epsilon, 0, \Pi, \Pi), \quad (\text{A7})$$

where

$$\epsilon = m_p n \left(1 + \frac{l_p^2}{r^2}\right), \quad (\text{A8})$$

$$\Pi = m_p n \frac{l_p^2}{2r^2}, \quad (\text{A9})$$

are the energy density and the pressure uniformly applied in the tangential direction to each sphere of constant radius, respectively, where $l_p = L_p/m_p$.

Appendix B: Coordinates on the celestial sphere of the distant observer

We review coordinates on the celestial sphere of the distant observer [35]. Let $e^{(a)}$ be a natural tetrad given as

$$e^{(0)} = \sqrt{1 - \frac{2\alpha}{r}} dt, \quad e^{(1)} = \left(1 - \frac{2m}{r}\right)^{-1/2} dr, \quad e^{(2)} = r d\theta, \quad e^{(3)} = r \sin\theta d\varphi, \quad (\text{B1})$$

which satisfy $g_{\mu\nu} = \eta_{ab} e^{(a)}{}_{\mu} e^{(b)}{}_{\nu}$, where $\eta_{ab} = \text{diag}(-1, 1, 1, 1)$. Then the tetrad components of the photon momentum, $k^{(a)} = e^{(a)}{}_{\mu} k^{\mu}$, are given by

$$k^{(0)} = (1 - 2\alpha/r)^{-1/2} (-k_t), \quad k^{(1)} = (1 - 2m/r)^{1/2} k_r, \quad k^{(2)} = k_{\theta}/r, \quad k^{(3)} = k_{\varphi}/(r \sin\theta). \quad (\text{B2})$$

These satisfy the null condition $\eta_{ab} k^{(a)} k^{(b)} = 0$, or equivalently,

$$(k^{(1)}/k^{(0)})^2 + (k^{(2)}/k^{(0)})^2 + (k^{(3)}/k^{(0)})^2 = 1. \quad (\text{B3})$$

Using this unit sphere at infinity, we define angle coordinates (ψ, β) on the celestial sphere as

$$k^{(1)}/k^{(0)}|_o = -\cos\beta, \quad k^{(2)}/k^{(0)}|_o = \sin\beta \sin\psi, \quad k^{(3)}/k^{(0)}|_o = -\sin\beta \cos\psi, \quad (\text{B4})$$

where β and ψ is the latitude and longitude, respectively, and the line-of-sight to the central black hole is $\beta = 0$. We can also introduce another angle coordinates as

$$X = -\frac{k^{(3)}}{k^{(0)}}|_o, \quad Y = \frac{k^{(2)}}{k^{(0)}}|_o. \quad (\text{B5})$$

Assume that the observer is far from the center $(r, \theta) = (r_o, \theta_o)$, where $r_o \gg M$. Then we can obtain the asymptotic forms of (X, Y) as

$$X \simeq -\frac{b}{r_o \sin\theta_o}, \quad (\text{B6})$$

$$Y \simeq \pm \frac{1}{r_o} \sqrt{q^2 - \frac{b^2}{\sin^2\theta_o}}, \quad (\text{B7})$$

where b and q are given in Eqs. (82) and (83), respectively. As a result, Eqs. (B6) and (B7) provide the relationship between (X, Y) and (b, q) .

When the observer is on the axis of $\theta_o = 0$ (or $\theta_o = \pi$), the coordinates (X, Y) are singular. Furthermore, $b/\sin\theta_o$ is indefinite for photons arriving at the axis. However, the latitude β is still valid because the indefinite quantities cancel out in the expression,

$$\beta \simeq \sin\beta = \sqrt{(k^{(2)}/k^{(0)})^2 + (k^{(3)}/k^{(0)})^2}|_o \simeq \frac{q}{r_o}. \quad (\text{B8})$$

This means that the observer on the axis can relate the angle β to q .

ACKNOWLEDGMENTS

The authors are grateful to Parth Bambhaniya, Dipanjan Dey, Minxi He, Hideki Ishihara, Satoshi Iso, Pankaj S. Joshi, Yasutaka Koga, Kazunori Kohri, Takahiko Matsubara, Kouji Nakamura, Ken-ichi Nakao, Keisuke Nakashi, Kenji Toma, Chul-Moon Yoo, and Hirotaka Yoshino for useful comments and helpful discussion. We would like to thank Andrea Maselli for their helpful comments on revisions to the manuscript. This work was supported by JSPS KAKENHI Grants No. JP19K14715 and No. JP22K03611 (TI); No. JP19K03876, No. JP19H01895, and No. JP20H05853 (TH); No. JP19H01900 and No. JP19H00695 (HS, YT).

-
- [1] A. Ghez, M. Morris, E. E. Becklin, T. Kremenek, and A. Tanner, The accelerations of stars orbiting the Milky Way’s central black hole, *Nature* **407**, 349 (2000) [arXiv:astro-ph/0009339].
 - [2] R. Schodel *et al.*, A Star in a 15.2 year orbit around the supermassive black hole at the center of the Milky Way, *Nature* **419**, 694 (2002) [arXiv:astro-ph/0210426].
 - [3] T. Do *et al.*, Relativistic redshift of the star S0-2 orbiting the galactic center supermassive black hole, *Science* **365**, 664 (2019) [arXiv:1907.10731 [astro-ph.GA]].
 - [4] H. Saida *et al.*, A significant feature in the general relativistic time evolution of the redshift of photons coming from a star orbiting Sgr A*, *Publ. Astron. Soc. Jpn.* **71**, 126 (2019) [arXiv:1910.02632 [gr-qc]].
 - [5] R. Abuter *et al.* (GRAVITY collaboration 2020), Detection of the Schwarzschild precession in the orbit of the star S2 near the galactic centre massive black hole, *Astron. Astrophys.* **636**, L5 (2020) [arXiv:2004.07187 [astro-ph.GA]].
 - [6] S. Weinberg, *Gravitation and Cosmology* (Wiley, New York, 1972).
 - [7] P. Gondolo and J. Silk, Dark matter annihilation at the galactic center, *Phys. Rev. Lett.* **83**, 1719 (1999) [arXiv:astro-ph/9906391].
 - [8] G. Bertone, M. Fornasa, M. Taoso, and A. R. Zentner, Dark matter annihilation around intermediate mass black holes: an update, *New J. Phys.* **11**, 105016 (2009) [arXiv:0905.4736 [astro-ph.HE]].
 - [9] L. Sadeghian, F. Ferrer, and C. M. Will, Dark matter distributions around massive black holes: A general relativistic analysis, *Phys. Rev. D* **88**, 063522 (2013) [arXiv:1305.2619 [astro-ph.GA]].
 - [10] T. Lacroix, Dynamical constraints on a dark matter spike at the Galactic Centre from stellar orbits, *Astron. Astrophys.* **619**, A46 (2018) [arXiv:1801.01308 [astro-ph.GA]].
 - [11] N. Bar, K. Blum, T. Lacroix, and P. Panci, Looking for ultralight dark matter near supermassive black holes, *JCAP* **07**, 045 (2019) [arXiv:1905.11745 [astro-ph.CO]].
 - [12] G. F. Rubilar and A. Eckart, Periastron shifts of stellar orbits near the galactic center, *Astron. Astrophys.* **374**, 95 (2001).
 - [13] T. Igata and Y. Takamori, Periapsis shifts in dark matter distribution with a dense core, *Phys. Rev. D*

- 105**, 124029 (2022) [arXiv:2202.03114 [gr-qc]].
- [14] D. Bini, F. De Paolis, A. Geralico, G. Ingrosso, and A. Nucita, Periastron shift in Weyl class spacetimes, *Gen. Rel. Grav.* **37**, 1263 (2005) [arXiv:gr-qc/0502062 [gr-qc]].
- [15] P. Bambhaniya, D. Dey, A. B. Joshi, P. S. Joshi, D. N. Solanki, and A. Mehta, Shadows and negative precession in non-Kerr spacetime, *Phys. Rev. D* **103**, 084005 (2021) [arXiv:2101.03865 [gr-qc]].
- [16] K. Ota, S. Kobayashi, and K. Nakashi, Revisiting timelike geodesics in the Fisher/Janis-Newman-Winicour-Wyman spacetime, *Phys. Rev. D* **105**, 024037 (2022) [arXiv:2110.07503 [gr-qc]].
- [17] A. Einstein, On a stationary system with spherical symmetry consisting of many gravitating masses, *Ann. Math.* **40**, 922 (1939).
- [18] A. Geralico, F. Pompei, and R. Ruffini, On Einstein clusters, *Int. J. Mod. Phys. Conf. Ser.* **12**, 146 (2012).
- [19] A. A. Nucita, F. De Paolis, G. Ingrosso, A. Qadir, and A. F. Zakharov, Sgr A*: a laboratory to measure the central black hole and cluster parameters, *Publ. Astron. Soc. Pac.* **119**, 349 (2007) [arXiv:0705.0494 [astro-ph]].
- [20] A. F. Zakharov, A. A. Nucita, F. De Paolis, and G. Ingrosso, Apoastron shift constraints on dark matter distribution at the Galactic Center, *Phys. Rev. D* **76**, 062001 (2007) [arXiv:0707.4423 [astro-ph]].
- [21] K. Iwata and C.-M. Yoo, Another approach to test gravity around a black hole, *Classical Quantum Gravity* **33**, 155007 (2016) [arXiv:1603.01762 [gr-qc]].
- [22] C. G. Boehmer and T. Harko, On Einstein clusters as galactic dark matter halos, *Mon. Not. R. Astron. Soc.* **379**, 393 (2007) [arXiv:0705.1756 [gr-qc]].
- [23] K. Lake, Galactic halos are Einstein clusters of WIMPs, arXiv:gr-qc/0607057.
- [24] V. Cardoso, K. Destounis, F. Duque, R. P. Macedo, and A. Maselli, Black holes in galaxies: Environmental impact on gravitational-wave generation and propagation, *Phys. Rev. D* **105**, L061501 (2022) [arXiv:2109.00005 [gr-qc]].
- [25] R. A. Konoplya, Black holes in galactic centers: Quasinormal ringing, grey-body factors and Unruh temperature, *Phys. Lett. B* **823**, 136734 (2021) [arXiv:2109.01640 [gr-qc]].
- [26] Z. Stuchlík and J. Vrba, Supermassive black holes surrounded by dark matter modeled as anisotropic fluid: epicyclic oscillations and their fitting to observed QPOs, *JCAP* **11**, 059 (2021) [arXiv:2110.07411 [gr-qc]].
- [27] K. Jusufi, Black holes surrounded by Einstein clusters as models of dark matter fluid, *Eur. Phys. J. C* **83**, 103 (2023) [arXiv:2202.00010 [gr-qc]].
- [28] E. Figueiredo, A. Maselli, and V. Cardoso, Black holes surrounded by generic dark matter profiles: Appearance and gravitational-wave emission, *Phys. Rev. D* **107**, 104033 (2023) [arXiv:2303.08183 [gr-qc]].
- [29] C. W. Misner and D. H. Sharp, Relativistic equations for adiabatic, spherically symmetric gravitational collapse, *Phys. Rev.* **136**, B571 (1964).
- [30] S. A. Hayward, Gravitational energy in spherical symmetry, *Phys. Rev. D* **53**, 1938 (1996) [arXiv:gr-

- qc/9408002].
- [31] R. M. Wald, *General Relativity* (The University of Chicago Press, Chicago, 1984).
 - [32] G. L. Comer and J. Katz, Thick Einstein shells and their mechanical stability, *Classical Quantum Gravity* **10**, 1751 (1993).
 - [33] J. Binney and S. Tremaine, *Galactic Dynamics: Second Edition* (Princeton University Press, Princeton, NJ USA, 2008).
 - [34] J. F. Navarro, C. S. Frenk, and S. D. M. White, The structure of cold dark matter halos, *Astrophys. J.* **462**, 563 (1996) [arXiv:astro-ph/9508025].
 - [35] J. M. Bardeen, Timelike and null geodesics in the Kerr metric, in *Black Holes (Les Astres Occlus)*, edited by C. Dewitt and B. S. Dewitt (Gordon and Breach, NewYork, 1973), pp. 215–239.
 - [36] G. Heißel, T. Paumard, G. Perrin, and F. Vincent, The dark mass signature in the orbit of S2, *Astron. Astrophys.* **660**, A13 (2022) [arXiv:2112.07778 [astro-ph.GA]].
 - [37] R. Abuter *et al.* (GRAVITY collaboration), Mass distribution in the Galactic Center based on interferometric astrometry of multiple stellar orbits, *Astron. Astrophys.* **657**, L12 (2022) [arXiv:2112.07478 [astro-ph.GA]].
 - [38] L. Hernquist, An analytical model for spherical galaxies and bulges, *Astrophys. J.* **356**, 359 (1990).